Final Draft
of the original manuscript:

Horstmann, J.; Thompson, D.R.; Monaldo, F.; Iris, S.; Graber, H.C.:
Can Synthetic Aperture Radars Be Used to Estimate Hurricane Force Winds?
In: Geophysical Research Letters (2005) AGU

DOI: 10.1029/2005GL023992

Can Synthetic Aperture Radars Be Used to Estimate Hurricane Force Winds?

J. Horstmann[1, 2], D. R. Thompson[3], F. Monaldo[3] and H. C. Graber[2]

J. Horstmann, GKSS Research Center, Institute for Coastal Research, Max-Planck-Str. 1, 21502 Geesthacht, Germany. (Horstmann@gkss.de)

[1]Institute for Coastal Research, GKSS Research Center, Germany.

[2]Center for Southeastern Tropical Advanced Remote Sensing, University of Miami, Florida, USA.

[3]Applied Physics Laboratory, Johns Hopkins University, Maryland, USA.

We compare wind fields retrieved from a RADARSAT-I synthetic aperture radar (SAR) image acquired over Hurricane Ivan on September 10, 2004 using the C-band geophysical model functions Cmod4 and its newest version Cmod5. Cmod4 has previously been shown to yield very good wind field estimates under low and moderate wind conditions. Wind directions obtained from streaks imaged by the SAR, that are well aligned with the mean surface wind direction are used to invert both algorithms to obtain estimates of the wind speed on scales as small as 1 km. These estimates are compared with predictions from a high-resolution tropical cyclone model as well as (sparse) local *in situ* data. It is found that the SAR wind speeds using Cmod5 agree reasonably well, while those from Cmod4 significantly under predict the wind speeds near the hurricane eye wall that reach values as high as 60 ms^{-1} or so.

1. Introduction

The ability of space borne microwave radars to measure the wind vector near the surface of the ocean relies on the fact that the near-surface wind field generates roughness (i.e. waves), which increases with wind speed. For radar backscatter at moderate incident angles, (roughly 20° to 60°), the normalized radar cross section (NRCS) is proportional to the spectral density of the surface roughness on the scales comparable to the radar wavelength. For this mid-incidence regime and wind speeds below 20 ms^{-1}, the NRCS is typically largest when the wind blows directly toward the radar and decreases to a minimum when the wind direction is orthogonal to the radar look direction. Another smaller maximum in NRCS occurs when the wind blows directly away from the radar.

The relation between the near-surface wind vector and NRCS can be described by an equation of the form

$$\sigma_0 = a(\theta)\, u^{\gamma(\theta)}\, (1 + b(u,\theta)\, \cos\Phi + c(u,\theta)\, \cos\, 2\Phi) \tag{1}$$

where σ_0 represents NRCS, u represents wind speed, Φ represents the relative angle between the radar look and wind direction, and θ is the nadir incidence angle. The quantities $a(\theta)$, $\gamma(\theta)$, $b(u,\theta)$ and $c(u,\theta)$ are empirical parameters determined by measured data.

Equation (1) shows that σ_0 is an exponential function of wind speed and a harmonic function of its direction. It is important to note that though the model function can relate wind speed and direction to NRCS, a specific NRCS value cannot be associated with a unique wind speed and direction pair. This significantly complicates the inversion from NRCS to wind speed. If wind direction is known *a priori*, it is possible to use Eq.(1) to estimate wind speed. An approach convenient for operational applications is to use

predicted wind directions from operational meteorological models *Monaldo et al.* [2004]. Another method is to estimate the wind direction directly using linear features in the SAR image itself *Horstmann et al.* [2002]. Both approaches have proven successful for moderate wind speed regimes.

In hurricanes, the surface roughness structure grows more complicated not only because of the addition of more wave breaking and surface foam, but also because of the more complex structure of the long wave field (cross seas) generated at previous times when the hurricane was at a different location. It is, therefore, likely that conventional empirical geophysical model functions (GMFs) developed using data for moderate wind conditions may also begin to break down.

In the following sections, we briefly describe some of the salient aspects of SAR wind retrieval schemes and the results of applying these in the high wind regimes observed in Hurricane Ivan. We will show that the newly-developed Cmod5 GMF [*Hersbach*, 2003] outperforms commonly used Cmod4 [*Stoffelen and Anderson*, 1997] in this high wind speed case study. In particular, we will show using NRCS measurements from a SAR image collected over Hurricane Ivan that the dependence of NRCS on the relative angle between the radar look direction and the local wind directions weakens, and perhaps disappears altogether, at very high wind speeds, and that such dependence is better modelled by the Cmod5 GMF.

2. SAR Wind Retrieval

2.1. Wind Direction Estimation

The most popular method for SAR wind direction retrieval is based on the imaging of linear features aligned along the wind direction [*Gerling*, 1986]. Most of these features are associated with wind streaks and marine atmospheric boundary layer (MABL) rolls, which are visible in SAR images at scales greater 200 m. To retrieve the orientation of these linear features, three methods have been developed: the Fast Fourier Transformation Method (FFT-Method) [*Gerling*, 1986; *Vachon and Dobson*, 1996; *Wackerman et al.*, 1996; *Lehner et al.*, 1998] the Local Gradient Method (LG-Method) [*Horstmann et al.*, 2002; *Koch*, 2004] and the Projection Method [*Wackerman et al.*, 2004]. Comparisons among these methods have shown that the LG-Method yields the smallest residuals, with a typical error of 18° [*Horstmann and Koch*, in press 2005]. Also investigations of the orientation of wind streaks at scales larger than 50 m with real aperture radar imagery have confirmed that wind streaks are very well aligned with the mean surface wind direction [*Dankert et al.*, 2003].

These results also suggest that wind direction retrievals are likely to be most accurate when linear features at the smallest possible scales visible from spaceborne SARs are used. These scales are typically 200 m, and are limited by the spatial resolution of the SAR system. Wind direction retrieval based on features whose scales are greater than 3 km can often represent to MABL rolls, whose orientations are more likely to differ significantly from the mean surface wind direction.

For the present investigation, the LG-Method is utilized to retrieve the SAR wind direction. In this approach, a SAR image is sequentially smoothed and reduced to resolutions of 100, 200 and 400 m. The resulting three SAR images retain spatial scales greater than

200, 400 and 800 m. From each of these images, local directions defined by the normal to the local gradient (to within a 180 ° ambiguity), are computed. In the next step, pixels associated with land, surface slicks, and sea ice, are masked and excluded from further analysis. From all of the retrieved directions, only the most frequent directions in a predefined grid cell are selected. These resulting wind directions typically vary by only a few degrees, except for cases where additional features are present in the SAR image, *e.g.,* ocean surface waves and artifacts from the original SAR processing. The 180° directional ambiguity can be removed if wind shadowing is present, which is often visible in the lee of coastlines. If such features are not present in the image other *a priori* information, *e.g.,* weather charts, atmospheric models or *in situ* measurements are used to remove ambiguities.

2.2. SAR Geophysical Model Functions

With the wind direction in hand, we can use the NRCS measured by the SAR to retrieve the wind speed using GMFs of the form given in Eq. (1). For C-band, VV-polarization NRCS, there are a number of popular model functions, for which the coefficients and exact model form have been determined empirically by using scatterometer (SCAT) data acquired by the European satellites ERS-1 and ERS-2 and co-located winds from the numerical model of the European Center for Medium-Range Weather Forecast. The most commonly used C-band model function is the Cmod4 [*Stoffelen and Anderson*, 1997] and the most recently developed is Cmod5 [*Hersbach*, 2003].

Each of these model functions is directly applicable for wind speed retrieval from C-band VV polarized SAR images [e.g. *Vachon and Dobson*, 1996; *Lehner et al.*, 1998;

Horstmann et al., 2003]. For wind speed retrieval from C-band SAR images acquired at HH-polarization (*i.e.,* the configuration for RADARSAT-1 images), no similar well-developed GMF exists. To meet this deficiency a hybrid model function is used that consists of one of the prior mentioned VV-polarization empirical models and a C-band polarization ratio [*Horstmann et al.*, 2000; *Thompson and Beal*, 2000; *Vachon and Dobson*, 2000]. The polarization ratio (PR) is defined as the ratio of HH-polarization NRCS to VV-polarization NRCS. The nature of the PR is an active area of research and several different PR's have been proposed in literature [*Thompson et al.*, 1998; *Mouche et al.*, in press 2005]. The PR proposed by *Thompson et al.* [1998] neglects wind speed and wind direction dependence and has the form

$$\mathrm{PR} = \frac{(1 + \alpha \tan^2 \theta)^2}{(1 + 2 \tan^2 \theta)^2}, \tag{2}$$

where α is a constant set to 0.6 to yield consistency with the measurements of *Unal et al.* [1991]. Several other values for α have been suggested in the literature for RADARSAT-1 and ENVISAT SAR data. These vary between 0.4 and 1.2 [*Horstmann et al.*, 2000; *Vachon and Dobson*, 2000; *Monaldo et al.*, 2002; *Horstmann and Koch*, in press 2005]. Comparisons of RADARSAT-1 SAR imagery produced from different SAR processing facilities showed that the different estimates of α may be due to the different calibrations of RADARSAT-1 SAR data at different facilities. Recently, *Mouche et al.* [in press 2005] have proposed a C-band PR , constructed using airborne RAR data acquired at C-band with both VV- and HH-polarization, that is also dependent on the wind direction.

Comparisons of C-band SAR retrieved wind speeds, using the Cmod4 at low to moderate wind speeds (up to 20 ms^{-1}) resulted in errors of $\sim$2 ms^{-1} [*Monaldo et al.*, 2002;

Horstmann et al., 2003; *Monaldo et al.*, 2004; *Horstmann and Koch*, in press 2005]. It is also well known that the Cmod4 underestimates the wind speeds at high winds (>20 ms^{-1}) when applied to SCAT and SAR data [*Donnelly et al.*, 1999; *Katsaros et al.*, 2002; *Horstmann et al.*, 2003]. The Cmod5 algorithm was specifically designed to provide better estimates of the NRCS at higher wind speeds [*Hersbach*, 2003]. It was constructed primarily using co-locations between ERS-2 SCAT backscatter triplets and first-guess model winds. For extremely high wind conditions, results from recent aircraft campaigns were also included [*Donnelly et al.*, 1999]. Differences between Cmod4 and Cmod5 for low to moderate wind speeds are relatively minor. At high wind speeds (>25 ms^{-1}) however, the differences become quite significant. In particular, the NRCS from Cmod4 continues to increases monotonically with wind speed for all incident angles, while that predicted by Cmod5 increases much more slowly with wind speed and for lower incident angles (25° to 30° depending on wind speed), can even reach a maximum value and decrease with further increase in wind speed. Furthermore, dependence of the NRCS on wind direction from Cmod5 becomes much weaker in the high wind regime compared to that of Cmod4.

3. High Wind Speed Dependence of the NRCS

A RADARSAT-1 SAR image of Hurricane Ivan, acquired on September 10, 2004 at 2307 UTC is shown in Fig. 1. This image is ideally suited to investigate the dependence of the C-band NRCS on wind speed and direction under extreme wind conditions. At the time of acquisition, Hurricane Ivan was situated about 80 km south of Kingston, Jamaica, and was classified by the US National Hurricane Center as a category 4 hurricane with maximum wind speeds on the order of 65 ms^{-1}. The color scale in Fig. 1 represents

NRCS values from the calibrated SAR image in the range -16 dB to -9 dB. The roughly circular hurricane eye is easily seen in the center of the figure where the NRCS is quite low. The variation of the NRCS with distance from the eye can be seen using the radii of the concentric circles shown in the figure. The NRCS increases dramatically at a distance of about 12 km from the eye, and remains roughly independent of the angular location around the eye for distances out to about 18 km. On a larger scale, one can also see in Fig. 1, evidence of counter-clockwise circulation from the wind streaks and rain bands.

To quantitatively investigate the wind direction dependence of the NRCS at various distances from the hurricane eye, we show in Fig. 2 the NRCS plotted as a function of azimuth angle in a clockwise direction around each of the concentric circles in Fig. 1 starting from 0° as shown at the top of that figure. Because of the cyclonic nature of the hurricane, these "circular transects" span all wind directions with respect to the antenna look direction. To reduce the effect of speckle noise in the transects, the NRCS was averaged over an area of $\approx$1 km^2. Note that the azimuth directions relative to the antenna look direction in the abscissa of the plot in Fig. 2 correspond roughly to the counter-clockwise wind directions expected in a (northern-hemisphere) hurricane. Thus, the directions 90° and 270° are approximately cross wind looks, while 0° and 180° are up and down wind, respectively. Note also that the different radii of the plots in Fig. 1 were selected carefully in order to avoid areas in the SAR image which are significantly affected by non-wind induced artifacts, *e.g.* rain bands.

Fig. 2 shows that for the plots with radii of 13 and 23 km, the NRCS is fairly constant around the entire circle. For these radii, the maximum change in NRCS over the entire

range is less than 1 dB. For the circle of $43km$ radius, the wind direction dependence of the NRCS plot begins to become apparent. In particular, this curve shows a wind direction dependence more similar to the second harmonic behavior seen in the standard model functions such as Cmod4. The 63 km plot shows an asymmetric dependence on wind direction. This asymmetry is partially due to the fact that the difference in incident angle between the near- and far-range is becoming significant for this case. (As shown in the plot at the bottom of Fig. 1, the difference in incident angle between the direction values of 90° and 270° is ≈7°.)

It is important to note from the Hurricane Ivan image of Fig. 1 that the backscatter NRCS in the high wind regime near the hurricane eye wall appears to be independent of wind direction. We show in the following section that this apparent loss of direction sensitivity, which is not well not represented by the Cmod4 model function, can have a large impact on the retrieved wind speeds in this regime.

4. Retrieved wind fields from Hurricane Ivan

As discussed in Section 2.2, differences between the Cmod4 and Cmod5 C-band GMFs can be significant for hurricane force winds. We have just seen in Section 3 that the SAR NRCS measured over Hurricane Ivan may in fact be more characteristic of behavior of Cmod5 than of Cmod4. To further investigate this issue, we have inverted the NRCS from the Ivan SAR image of Fig. 1 to produce two wind maps based on the Cmod5 and Cmod4 model functions and shown in left and center panels of Fig. 3, respectively. For both inversions, we have used the LG-Method to determine the wind directions and the PR given by Eq. (2) with $\alpha = 0.6$. From an examination of the first two panels in Fig. 3,

differences between the two GMFs are immediately clear. Perhaps most obvious is the fact that Cmod5 yields significantly higher winds than does Cmod4; 50 to 55 ms^{-1} versus 25 to 30 ms^{-1}, respectively. As mentioned earlier, the maximum wind speed reported by the National Hurricane Center for Ivan at the overpass time was about 65 ms^{-1}. We see from Fig. 3 that the predicted winds from Cmod5 are fairly close to this value, while those from Cmod4 are significantly lower. The right-hand panel of this figure shows the difference image (Cmod5 - Cmod4). Notice the large differences especially near the north-east hurricane eye wall where the maximum winds are expected.

The small circular dots shown at the tips of the wind vectors on the Cmod5 and Cmod4 wind maps represent wind speeds predicted by an interactive objective kinematic analysis (IOKA) model for tropical cyclones described in *Cox et al.* [1992]. These dots are color coded using the same wind speed scale as the SAR map so that they become less visible in regions where the agreement between the model and the extracted SAR wind speed is good. One can see that the agreement is generally good for the Cmod5 map; especially in the higher wind region near the eye wall, while for the Cmod4 wind map, it is significantly worse.

It is also apparent from Fig. 3 that the angular dependence of the predicted wind speeds associated with Hurricane Ivan is closer to the expected behavior. In particular, the Cmod5 wind speeds near the hurricane eye are not only larger than those from Cmod4, but they are much more uniform around the full angular extent of the eye. To see this effect more clearly, we show in Fig. 4 plots of the predicted NRCS versus wind direction for Cmod5 (a) and Cmod4 (b) that would occur around the concentric circles in Fig. 1.

These curves should be compared with the corresponding curves in Fig. 2 extracted directly from the NRCS data from Hurricane Ivan shown in Fig. 1. Note that the curves computed from Cmod5 compare reasonably well with the corresponding curves in Fig. 1. The Cmod4 curves in Fig. 4 b) show more sensitivity to wind direction at the higher wind speeds, and are generally rather different from those computed using Cmod5. We remind the reader that the asymmetry about 180° apparent in the NRCS predictions of both GMFs in Fig. 4 is due to the fact that the incident angle varies around the concentric circles in Fig. 1. As mentioned already in Section 3, this variation of the incident angle (as well as the fact that wind may not be constant) also affects the angular dependence of the "circular transects" in Fig. 2. The extent of this variation is shown in Fig. 4 c). The results shown in Fig. 4 further confirm our conclusions based on the wind maps in Fig. 3 that the Cmod5 GMF provides a better representation of the hurricane Ivan wind field.

5. Conclusion and Outlook

To the best of our knowledge, this letter describes the first attempt to extract quantitative wind speed estimates under hurricane conditions using the recently developed Cmod5 GMF. At least for this single case, we conclude that Cmod5 provides better wind speed estimates for hurricane force winds than the more commonly used Cmod4. The major difference between these two GMFs is that for Cmod5, the NRCS (at a particular incident angle) becomes rather insensitive to the local wind vector (speed and direction) for winds >25 ms^{-1}. This high-wind dependence is quite different from that of Cmod4, and as we have attempted to demonstrate in this letter, can have a major impact on the

extracted wind field for the extreme conditions such as those of Hurricane Ivan. Although the Cmod5 GMF was developed empirically, its loss of wind sensitivity at high wind speeds has a more fundamental basis. In a recent letter, *Donelan et al.* [2004] showed that the aerodynamic roughness (*i.e.* the drag coefficient) over the ocean approaches a limiting value in high wind conditions. This behavior is significantly different from its behavior at intermediate wind speeds where the drag coefficient increases with wind speed. Qualitatively, the wind speed dependence of the NRCS predicted by Cmod5 mirrors that observed for the drag coefficient.

Much work remains to be done to further refine wind estimation of hurricane force winds. It is clear that more cases are needed to substantiate the findings for Hurricane Ivan discussed here. Also, the issue of the proper C-band GMF for HH-polarization, discussed in Section 2.2, must be resolved. To begin to address this issue, we have ordered a VV-polarization EnviSAT SAR image collected over Hurricane Isabel to compare with the HH-polarization image discussed here. We will examine this image to see if the same general conclusions found for the HH-polarization image still apply. The use of high-resolution SAR wind mapping under extreme wind conditions is just beginning to be recognized as a viable tool for hurricane tracking and prediction. Although much work remains to be done, we believe that the potential payoff is well worth continued effort.

Acknowledgments. The authors thank Steve Iris of the Canadian Space Agency and Radarsat International for their collaboration with CSTARS in the Hurricane Watch program to receive RADARSAT-1 data. The National Oceanographic Partnership Pro-

gram (NOPP) provided high-resolution wind fields from numerical models. This study, CSTARS and the NOPP are supported by funding from the Office of Naval Research.

References

Cox, A., J. Greenwood, V. Cardone, and V. Swail (1992), An interactive objective kinematic analysis system, in *Fourth Int. Workshop on Wave Hindcasting*.

Dankert, H., J. Horstmann, and W. Rosenthal (2003), Ocean wind fields retrieved from radar-image sequences, *J. Geophys. Res.*, *108(C11)*(C11), 3352, doi: 10.1029/2003JC002,056.

Donelan, M., B. K. Haus, N. Reul, W. J. Plant, M. Stiassnie, H. C. Graber, O. B. Brown, and E. S. Saltzman (2004), On the limiting aerodynamic roughness of the ocean in very strong winds, *Geophys. Res. Lett*, *31, 18306,doi:10.1029/2004GL019460*.

Donnelly, W., J. Carswell, R. McIntosh, P. Chang, and J. Wilkerson (1999), Revised ocean backscatter models at C and Ku band under high wind conditions, *J. Geophys. Res.*, *104*, 11 485–11 498.

Gerling, T. (1986), Structure of the surface wind field from Seasat SAR, *J. Geophys. Res.*, *91*, 2 308–2 320.

Hersbach, H. (2003), CMOD5 an improved geophysical model function for ERS C-band scatterometry, *Internal report*, European Centre for Medium-Range Weather Forecast.

Horstmann, J., and W. Koch (in press 2005), Measurement of ocean surface winds using synthetic aperture radars, *J. Oceanic Eng.*

Horstmann, J., W. Koch, S. Lehner, and R. Tonboe (2000), Wind retrieval over the ocean using synthetic aperture radar with C-band HH polarization, *IEEE Trans. Geosci.*

Remote Sens., *38*(5), 2 122–2 131.

Horstmann, J., W. Koch, S. Lehner, and R. Tonboe (2002), Ocean winds from RADARSAT-1 ScanSAR, *Can. J. Remote Sens.*, *28*(3), 524–533.

Horstmann, J., H. Schiller, J. Schulz-Stellenfleth, and S. Lehner (2003), Global wind speed retrieval from SAR, *IEEE Trans. Geosci. Remote Sens.*, *41*(10), 2277–2286.

Katsaros, K., P. Vachon, W. Lio, and P. Black (2002), Microwave remote sensing of tropical cyclones from space, *J. of Oceanography*, *58*, 137–151.

Koch, W. (2004), Directional analysis of SAR images aiming at wind direction, *IEEE Trans. Geosci. Remote Sens.*, *42*(4), 702–710.

Lehner, S., J. Horstmann, W. Koch, and W. Rosenthal (1998), Mesoscale wind measurements using recalibrated ERS SAR images, *J. Geophys. Res.*, *103*, 7 847–7 856.

Monaldo, F., D. Thompson, R. Beal, W. Pichel, and P. Clemente-Colon (2002), Comparison of SAR-derived wind speed with model predictions and ocean buoy measurements, *IEEE Trans. Geosci. Remote Sens.*, *39*(12), 2587–2600.

Monaldo, F., D. Thompson, W. Pichel, and P. Clemente-Colon (2004), A systematic comparison of QuikSCAT and SAR ocean surface wind speeds, *IEEE Trans. Geosci. Remote Sens.*, *42*(2), 283–291.

Mouche, A., D. Hauser, J.-F. Daloze, and C. Gurin (in press 2005), Dual polarization measurements at C-band over the ocean: Results from airborne radar observations and comparison with ENVISAT ASAR data, *IEEE Trans. Geosci. Remote Sens.*

Stoffelen, A., and D. Anderson (1997), Scatterometer data interpretation: Estimation and validation of the transfer function CMOD4, *J. Geophys. Res.*, *102*, 5 767–5 780.

Thompson, D., and R. Beal (2000), Mapping of mesoscale and submesocale wind fields using synthetic aperture radar, *John Hopkins APL Tech. Dig.*, *21*(1), 58–67.

Thompson, D., T. Elfouhaily, and B. Chapron (1998), Polarization ratio for microwave backscattering from the ocean surface at low to moderate incidence angles, in *Proc. Int. Geosci. Remote Sens. Symp. 1998*, Seattle, USA.

Unal, C., P. Snoeij, and P. Swart (1991), The polarization-dependent relation between radar backscatter from the ocean surface and surface wind vectors at frequencies between 1 and 18 GHz, *IEEE Trans. Geosci. Remote Sens.*, *29*, 621–626.

Vachon, P., and F. Dobson (2000), Wind retrieval from RADARSAT SAR images: Selection of a suitable C-band HH polarization wind retrieval model, *Can. J. Remote Sens.*, *26*(4), 306–313.

Vachon, P. W., and F. Dobson (1996), Validation of wind vector retrieval from ERS-1 SAR images over the ocean, *Global Atmos. Ocean Syst.*, *5*, 177–187.

Wackerman, C., C. Rufenach, R. Schuchman, J. Johannessen, and K. Davidson (1996), Wind vector retrieval using ERS-1 synthetic aperture radar imagery, *J. Geophys. Res.*, *34*, 1 343–1 352.

Wackerman, C., W. Pichel, and P. Clemente-Colón (2004), A projection method for automatic estimation of wind vectors with RADARSAT SAR imagery, *ESA SP-Series*, *SP-565*, 55–60.

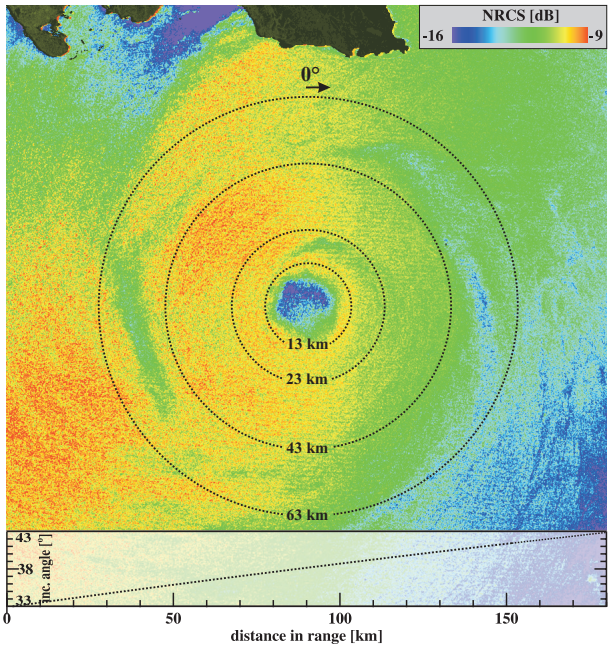

Figure 1. SAR image acquired by the Canadian RADARSAT-1 satellite on September 10, 2004 at 2307 UTC showing the surface signature of Hurricane Ivan. The radii of the dotted circles, centered at hurricane eye, are shown on the figure. The plot beneath the image shows the incident angle as a function of distance across the image. This image was received and processed at CSTARS.

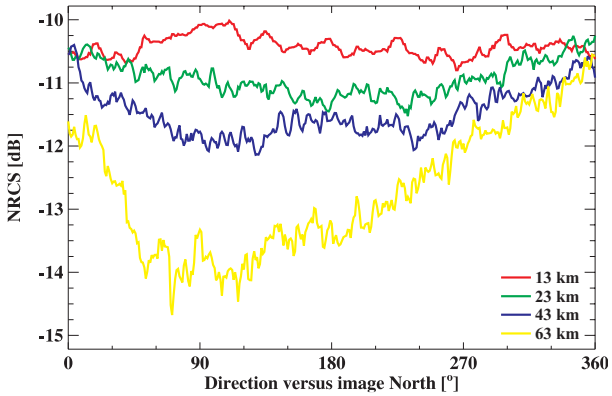

Figure 2. NRCS versus direction around the concentric circles in the SAR image of Fig. 1.

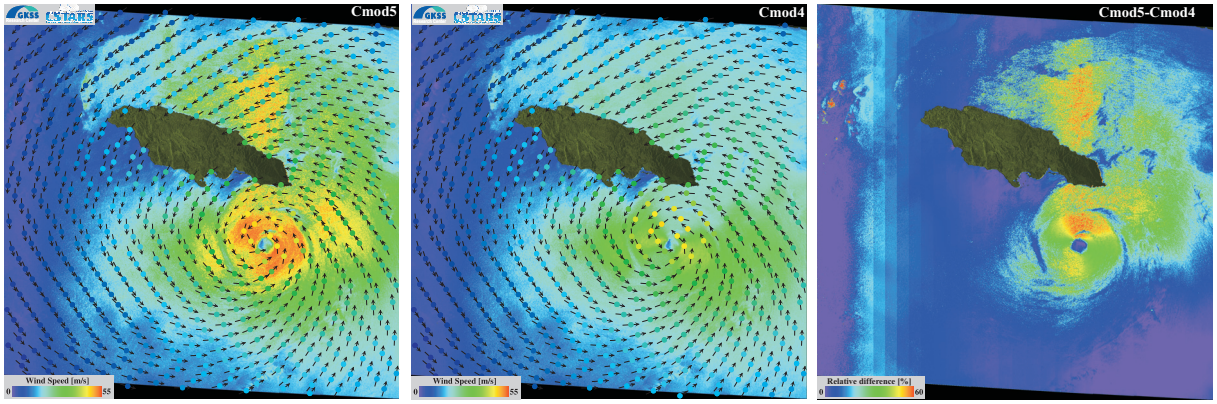

Figure 3. SAR wind map from the Cmod5 inversion (left panel), from Cmod4 (center panel), and the differences Cmod5 - Cmod4 (right panel). For both inversions, we have used the LG-Method to determine the wind directions and Eq. (2) with $\alpha = 0.6$ for the polarization ratio.

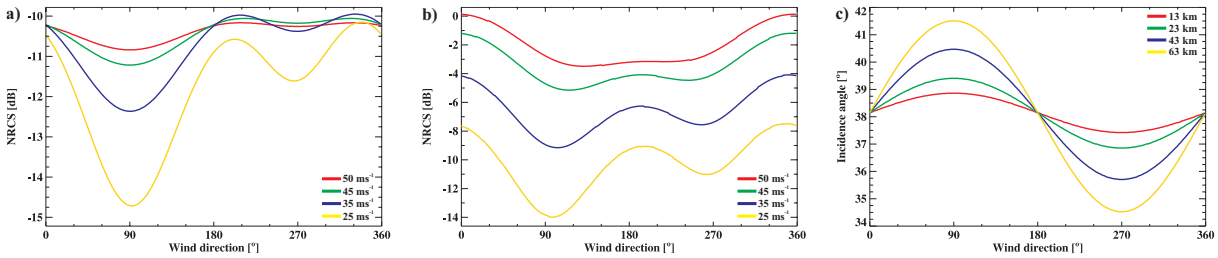

Figure 4. NRCS values versus wind direction from the Cmod5 (a)) and Cmod4 (b)) for the constant wind speeds shown in the legend. For both cases, Eq. (2) with $\alpha = 0.6$ was used for the polarization ratio. In c) the variation in incident angle with wind direction for each case is plotted. The curves in this figure complement the data for the concentric circles in Fig. 1 as shown by the plots in Fig. 2.